INTERNATIONAL JOURNAL OF AUTOMOTIVE AND MECHANICAL ENGINEERING (IJAME)
ISSN: 2229-8649 e-ISSN: 2180-1606
VOL. 18, ISSUE 4, 9271 – 9283
DOI: https://doi.org/10.15282/ijame.18.4.2021.10.0713

ORIGINAL ARTICLE

Analysis of the Influence of Droplet Breakup Time using Kelvin-Helmholtz Model, on the Diesel Spray Formation, Evaporation and Combustion

Y. Ortiz Sanchez[1,*], E. G. Florez[2] and D. H. Mesa[1]

[1]Facultad de Tecnología Mecánica, Universidad Tecnológica de Pereira, 660003 Pereira, Risaralda, Colombia
Phone: +573203815992
[2]Facultad de ingeniería y Arquitectura, Universidad de Pamplona, 543050 Pamplona, Norte de Santander, Colombia

ABSTRACT – A numerical simulation of the intake and compression stroke and fuel spray and combustion in a direct injection compression ignition engine was performed using the Converge CFD software. For this purpose, the Reynolds Average Navier-Stokes (RANS) k-e RNG model and an n-dodecane kinetic mechanism were used in order to obtain the flow fields in the cylinder and to perform the breakup time analysis of the Kelvin-Helmholtz model in the variables related to the spray and combustion. The turbulent flow inside the cylinder was analysed, obtaining consistent results with experimental pressure data and other research authors. The droplet breakup time is evaluated as a function of the breakup time constant (B1), the initial droplet radius (r_o), the wavelength (Λ_{KH}) and the maximum growth rate (Ω_{KH}). The results indicate that the numerical method and the models used in this work are adequate to perform subsequent representative combustion analyses with values of B1=7. It was possible to show that the formation of the species OH is greater for low values of B1. Also, higher values of the breakup time, variables such as temperature, pressure, fuel evaporation, ignition delay, and species formation are affected.

ARTICLE HISTORY
Received: 31st Dec 2020
Revised: 7th Oct 2021
Accepted: 10th Nov 2021

KEYWORDS
Turbulent flow;
Fuel evaporation;
Droplet breakup;
Droplet breakup time;
Compression ignition engine

INTRODUCTION

The energy crisis due to fossil fuel depletion, its resulting fluctuation of prices and the increasingly demanding regulations against emissions have encouraged research on alternative fuels. The first bio-fuel studied was biodiesel, but the production of biodiesel is expensive compared to other emerging options like straight vegetable oil (SVO). Several researchers have focused on different biodiesel properties and their behaviour during combustion in a diesel engine [1-7]. Flow conditions inside the cylinder of an internal combustion engine are mainly generated by air input through the valves during the intake stroke and later by the compression stroke. In the intake system, pressure waves move back and forth from the cylinder to the inlet. If the waves are in phase, they are reinforced while if the waves are out of phase, they are cancelled. The magnitudes of the variables that define the flow within the cylinder can be obtained experimentally or by means of numerical simulation. The movement of air inside the cylinder is an important factor in the combustion of a diesel engine since it contributes to the quality of the fuel-air mixture and the formation of soot and particulate material in the combustion as well.

The parameters of intake and compression strokes allow the quantification of various fluid-dynamic phenomena during engine operation, such as the instantaneous discharge coefficient C_{Di}, which is the ratio between the actual flow of air through the intake valve ($\dot{m}$) and the ideal flow obtained for an isentropic expansion through the same passage area [8]. The flow within the cylinder is generally characterised by movements known as Swirl and Tumble. Swirl represents the rotary movement of the gas around the z-axis of the cylinder, contributing to the improvement of the fuel-air mixture; such movement is quantified by the Swirl ratio (R_s), given by Eq. (1), [9], [10].

$$R_s = \frac{\Omega_{flow}}{\Omega_{crank}} \tag{1}$$

where, Ω_{flow} is the flow rotation speed and Ω_{crank} is the crank rotation speed, both expressed in rad/s. Likewise, at the end of the compression stroke, when the piston approaches the top dead center (TDC), there is a radial movement called Squish within the cylinder, which in turn generates a secondary rotational flow around the x or y-axes (Tumble). A similar equation defines the Tumble ratio as the division of the rotation speed of the flow around the x-axis or y-axis over the rotation speed of the crank.

In the literature, the flow in the intake manifold of a diesel engine has been analysed experimentally and numerically by authors in [11], who concluded that acoustic characteristics influence the engine torque and that the dynamic behaviour of the intake manifold is related to the propagation of pressure waves in the manifold. Furthermore, Malkhede and Khalane [12] showed that higher speeds in the intake manifold increase the pressure oscillation amplitude, which enhances volumetric efficiency as long as the closing movement of the valve is synchronised with the pressure oscillation.

*CORRESPONDING AUTHOR | Y. Ortiz Sanchez | ✉ yosanchez@utp.edu.co

On the other hand, Nguyen et al. [13] obtained numerical results of the pressure inside the manifold and provided the corresponding validation with experimental data.

As far as the flow inside the cylinder is concerned, Subramanian et al. [14], Perini et al. [15], and Rathore et al. [16], numerically simulated the effect of pistons of different shapes on the movement and flow turbulence inside the cylinder in a diesel engine, using Fluent, with Reynolds Average Navier-Stokes (RANS) k-e and k-e RNG turbulence models. Concluding that the piston, with a cup configuration, generates a high swirl at the end of the compression stroke, hence high volumetric efficiency. According to these studies, the discharge coefficient increases with the elevation of the valve and that there is a recirculation of air on the opposite side of the intake valve, due to the interaction of the flow with the cylinder wall. These numerical results were validated with experimental results.

In the admission and compression strokes, for a direct injection engine, Maurya and Mishra [17] simulated the air-fluid dynamics with STAR-CD software, applying the k-e RNG model, the respective results obtained for the Swirl ratio, radial velocity and turbulent intensity inside the cylinder, were validated with experimental data acquired through laser doppler velocimetry (LDV). Similarly, Gold et al. [18] simulated a direct injection diesel engine, applying the k-e and k-w SST turbulence models, observed squish enhancement in compression due to engine geometry and fluid rotation due to helical intake manifold (Swirl). Finally, Payri et al. [19] simulated the intake and compression strokes in a direct injection diesel engine with different combustion chambers, validating their results with LDV for different piston shapes, finding that cup-shaped piston favours the generation of swirl at the end of the compression stroke.

In a diesel engine, the formation, droplets breakup and evaporation determine combustion rate and ignition delay. Therefore, the simulation of fuel droplet breakup and fuel spray evaporation leads to the understanding of the influence of the spray-on combustion efficiency and pollutant emission. With a detailed characterisation of fuel evaporation and combustion, it is possible to optimise the injection system and the geometry of the combustion chamber. Kong et al. [20] performed numerical simulation and experimental validation of turbulent flow inside an engine, integrated with spray breakup, ignition and droplet interaction models. They showed that droplet breakup time is related to the initial disturbance level in the breakup process. Furthermore, experimentally, Yao et al. [21] performed spray combustion tests using n-dodecane, evaluating the influence of injection temperature on spray penetration and ignition delay. n-dodecane is commonly used as a fuel surrogate for simulation of combustion in diesel engines due to similar characteristics to diesel oil [22]. Besides, the numerical simulation of spray combustion of n-dodecane using Large-eddy simulation (LES) was done by Wehrfritz et al. [23] with a detailed kinetics mechanism in OpemFOAM, identifying two ignition states, one in the lean mixture and the other in the rich mixture.

For the analysis of the influence of the swirl ratio on mixture formation, Tulwin et al.[24] simulated the combustion in a Diesel engine using the VECTIS software with k-e RNG turbulence model and KH-RT breakup model. They observed that the highest pressure was obtained with a swirl ratio of 1.5, which contributed to a better mixture formation. Likewise, Zhou et al. [25] simulated spray combustion of four diesel surrogates, including n-dodecane, using LES in KIVA3v software and the KH-RT model for droplet breakup. They found that ignition delay and flame lift-off length are dependent on the variables of the model. Yousefifard et al. [26] compared experimental results against spray and combustion simulation. In their simulation, 20 is the most appropriate value of the breakup time constant (B_1) for the Kelvin-Helmholtz-Rayleigh-Taylor (KH-RT) model. Similarly, the breakup time for this model was analysed by Gao et al. [27]. They conclude that the breakup time decreases with the pressure in the combustion chamber, affecting the droplet size. Another analysis of the breakup time in the KH-RT model was performed by Srivastava and Jaberi [28], resulting in an increase of the liquid spray length as the breakup time increases. Finally, Kim et al. [29] analysed the dependence of the spray characteristics on the physical-chemical properties of the fuel, using a computational fluid dynamic (CFD) model with n-dodecane and KH-RT droplet-breakup model. They showed that the physical-chemical properties of the fuel affect spray penetration and ignition delay.

SVO and its derivatives might be directly used in the ignition by compression engines with a significant cost reduction and mitigation of the impact of life cycles associated with fuel usage and processing. Nevertheless, the design of current engines poses operation limitations with these alternative fuels. Thus, it is required to study engine operation with SVO since diesel fuel and SVO does not share the same thermo-physical and thermochemical properties [30]. In recent years, the growing interest in SVO usage in diesel motors has led to studies on evaporation and droplets formation of this type of fuel, as well as other processes [31], [32]. Unfortunately, there are few documented works on SVO spray combustion simulation in diesel engines. As a first step in pursuing the aforementioned simulation, it is necessary for a numerical model capable of reliable results. This work aims to identify the appropriate simulation model and its corresponding sub-models with a focus on the turbulent interaction and droplet breakup.

The numerical simulation of the intake, exhaust and evaporation of the fuel spray in a compression-ignition engine, operating with diesel fuel, was carried out using Converge CFD software and considering turbulent and compressible flow with RANS equations and k-e RNG turbulence model. For the combustion simulation, an n-dodecane kinetic mechanism ($C_{12}H_{26}$) was used in a single-cylinder direct-injection engine at 1800 rpm, considering all the phenomenology of a three-dimensional flow. Subsequently, spray and combustion were simulated to analyse the influence of the breakup time of the KH-RT model on the breakup and evaporation of the fuel droplets. The fuel spray parameters such as droplet diameter, ignition delay, heat release rate and chemical species formation were used. The average values of the flow variables, the field of flow variables, and the spray were obtained from the simulation. The model was then validated with experimental pressure data in the engine and with results obtained by other researchers in numerical simulations.

THEORETICAL BACKGROUND

The numerical simulation of fuel flow and spray in an internal combustion engine is supported by a set of differential and parametric equations that must be solved with input parameters, initial conditions and boundary conditions.

Turbulent Flow

To obtain speed, temperature and pressure fields in a compressible flow, it is necessary to solve the equations of conservation of mass, conservation of momentum (Navier-Stokes Equations), energy conservation, and gases in the following equation [33].

$$\frac{p}{\rho} = Z\frac{R}{W}T \tag{2}$$

where, p is the pressure, ρ is the density, Z is the compressibility factor (1.0 for the ideal gas), R is the gas constant, W is the molecular weight, and T is the temperature.

The methods for numerically solving the Navier-Stokes equations to describe turbulent flow, commonly used today, are: Direct Numerical Simulation (DNS), Large Eddy Simulation (LES), and Reynolds Averaged Navier-Stokes (RANS). The RANS modelling for compressible flow is based on the decomposition of the Navier-Stokes equations, substituting in them an instantaneous velocity. This can be calculated from the sum of the average velocity and the fluctuation of the velocity, [34] or by using Favre averaging, which expresses that any flow property is the sum of an average quantity and its fluctuation, weighted by the mass, e.g. the instantaneous velocity u_i in Eq.(3), can be written as the sum of an average value $\widetilde{u_\iota}$ and a fluctuation u_i'' [35], [36].

$$u_i = \widetilde{u_\iota} + u_i'' \tag{3}$$

Equations (4), (5) and (6) correspond to the conservation of mass, amount of motion and energy, in terms of the Favre averaging, respectively. [9]:

$$\frac{\partial\overline{\rho}}{\partial t} + \frac{\partial\overline{\rho\widetilde{u_\iota}}}{\partial x_i} = 0 \tag{4}$$

$$\frac{\partial\overline{\rho}\widetilde{u_\iota}}{\partial t} + \frac{\partial\overline{\rho}\widetilde{u_\iota}\widetilde{u_j}}{\partial x_j} = -\frac{\partial\tilde{p}}{\partial x_i} + \frac{\partial}{\partial x_j}\left(-\overline{\rho u_\iota'' u_j''}\right) + \frac{\partial}{\partial x_j}\left[\mu\left(\frac{\partial\widetilde{u_\iota}}{\partial x_j} + \frac{\partial\widetilde{u_j}}{\partial x_i}\right) - \frac{2}{3}\mu\frac{\partial\widetilde{u_k}}{\partial x_k}\delta_{ij}\right] \tag{5}$$

$$\frac{\partial\overline{\rho\tilde{e}}}{\partial t} + \frac{\partial\widetilde{u_j}\overline{\rho}\tilde{e}}{\partial x_j} = -p\frac{\partial\widetilde{u_j}}{\partial x_j} + \frac{\partial}{\partial x_j}\left(K\frac{\partial\tilde{T}}{\partial x_j}\right) + \sigma_{ij}\frac{\partial\widetilde{u_\iota}}{\partial x_j} + \frac{\partial}{\partial x_j}\left(\overline{\rho}D\sum_m \widetilde{h_m}\frac{\partial Y_m}{\partial x_j}\right) + S \tag{6}$$

where, Y_m is the mass fraction of species m, D is the mass diffusivity, K is the thermal conductivity, e is the specific internal energy, h_m is the enthalpy of species m, S is the source term and σ_{ij} is the stress tensor. From the above equations, an additional term called Reynolds' Tensor is obtained ($R_{ij} = -\overline{\rho u_\iota'' u_j''}$); composed of six scalar unknowns, generating a problem to close the system of equations.

RANS equations can be solved in two ways; with transport equation models for each of the R_{ij} term (Reynolds Stress Models - RSM), or by using turbulent viscosity models, based on the Boussinesq hypothesis to express Reynold´s tensor; which in terms of Favre averaging, given by Eq. (7).

$$R_{ij}\mu_t = \left(\frac{\partial\widetilde{u_\iota}}{\partial x_j} + \frac{\partial\widetilde{u_j}}{\partial x_i}\right) - \frac{2}{3}\delta_{ij}\left(\rho k + \mu_t\frac{\partial\widetilde{u_\iota}}{\partial x_i}\right) \tag{7}$$

where, μ_t is the turbulent viscosity. To represent the turbulent viscosity (μ_t), different turbulence models are considered, such as the k-e model, the k-e RNG model, the k-w model, among others. In this work, the k-e RNG model was used because it offers better results in the simulation of combustion processes, [14]–[16], where the turbulent viscosity is obtained from Eq. (8), [35].

$$\mu_t = C_\mu\rho\frac{k^2}{\varepsilon} \tag{8}$$

here, C_μ is turbulence constant of the model, k is the turbulent kinetic energy obtained from Eq.(9), and ε is the rate of dissipation of turbulent kinetic energy, calculated from Eq. (10).

$$\frac{\partial \rho k}{\partial t} + \frac{\partial \rho \widetilde{u_j} k}{\partial x_j} = R_{ij}\frac{\partial \widetilde{u_i}}{\partial x_j} - \rho\varepsilon + \frac{\partial}{\partial x_j}\left[\left(\mu + \frac{\mu_t}{Pr_k}\right)\frac{\partial k}{\partial x_j}\right] + S_k \tag{9}$$

$$\frac{\partial \rho \varepsilon}{\partial t} + \frac{\partial \rho \widetilde{u_j} \varepsilon}{\partial x_j} = \frac{\partial}{\partial x_j}\left(\frac{\mu_t}{Pr_\varepsilon}\frac{\partial \varepsilon}{\partial x_j}\right) + C_{\varepsilon 3}\rho\varepsilon\frac{\partial \widetilde{u_i}}{\partial x_i} + \left(C_{\varepsilon 1}\frac{\partial \widetilde{u_i}}{\partial x_j}R_{ij} - C_{\varepsilon 2}\rho\varepsilon + c_k S_k\right)\frac{\varepsilon}{k} + S - \rho R \tag{10}$$

where, Pr_k and Pr_ε are Prandtl's numbers for turbulent flow, $C_{\varepsilon 1}$, $C_{\varepsilon 2}$, $C_{\varepsilon 3}$ are model coefficients, S_k is the source term representing the iterations with the discrete phase (spray), S is a source term provided by the user.

Spray Breakup and Drop Vaporisation

The injected fuel into the cylinder disintegrates along its jet axis and evaporates to generate the fuel-air mixture [37]. The turbulent and rotational movement of the gas inside the cylinder is a factor that greatly influences the jet of injected fuel and the formation of the spray. These phenomena in the fluid affect the penetration of the fuel spray since it depends on two opposing forces, which are the initial kinetic energy of the jet and the aerodynamic resistance of the gases [8], [37]. In droplet breakup, the Blob injection model for the primary breakup considers that drops are initially injected with a diameter equal to the diameter of the injector nozzle. Subsequently, these drops undergo a secondary breakup process. Kelvin Helmholtz's model of secondary breakup considers the rate of change of the droplet radius in the main (or parent) portion, and when the secondary breakup occurs, as given by Eq. (11). In this breakup model, the initial diameter is given by the Blob model.

$$\frac{dr_o}{dt} = -\frac{r_o - r_c}{\tau_{KH}} \tag{11}$$

where, r_o is the initial droplet radius, r_c is the droplet radius resulting from the breakup and τ_{KH} is the breaktime.

$$\tau_{KH} = \frac{3{,}726 B_1 r_o}{\Lambda_{KH}\Omega_{KH}} \tag{12}$$

where, B_1 is the breakup time constant, Ω_{KH} is the maximum growth rate (or the most unstable wave) and Λ_{KH} is the wavelength. For diesel fuel simulation, B_1 is recommended as 7 in Converge CFD and is also recommended as 10 by Reitz [38] and Kong et al. [20]. For large values of B_1, the breakup time (τ_{KH}) is greater, and therefore from Eq.(11), the new droplets that arise from the secondary breakup process are of larger radius than when small values of B_1 are used, and consequently, the formation of small droplets is slower. Once the fuel is injected into the cylinder, it starts to evaporate as the heat transferred to the droplets increases the temperature of the cylinder and fuel vapour forms on the surface of the droplet [37].

The droplet evaporation model, using Frossling correlation, expresses the ratio of droplet radius change, due to evaporation, as in Eq. (13).

$$\frac{dr}{dt} = -\frac{\rho_g D}{2\rho_l r}B_d Sh_d \tag{13}$$

where, D is the mass diffusivity, B_d is the mass transfer number given by Eq.(14) and Sh_d is the Sherwood number given by Eq (15).

$$B_d = \frac{Y_1^* - Y_1}{1 - Y_1^*} \tag{14}$$

$$Sh_d = \left(2 + 0{,}6 Re_d^{1/2} Sc^{1/3}\right)\frac{ln(1 + B_d)}{B_d} \tag{15}$$

where, Y_1^* is the mass fraction of the vapour on the surface of the droplet, Y_1 is the mass fraction of the vapour, Re_d is Reynold´s number of the droplet, Sc is the Schmidt number. To calculate the temperature of the droplet, the droplet evaporation model Eq. (16) is used, which defines that the energy delivered to the droplet can be used to heat it or to evaporate it.

$$\overline{A}_d Q_d = c_l m_d \frac{dT_d}{dt} - \frac{dm_d}{dt}H_{vap} \tag{16}$$

where, Q_d is the heat flow by conduction on the surface of the droplet per unit area, c_l is the specific heat of the liquid, T_d is the temperature of the droplet, m_d is the mass of the droplet, H_{vap} is the latent heat of vaporisation, $\overline{A}_d$ is the middle area of the droplet.

Turbulent Combustion

Combustion in a diesel engine is described by ignition delay, premixed combustion, non-premixed combustion (mixing-controlled combustion), and final combustion. Flame lift-off means that the combustion reaction is confined to a small area of thickness compared to the combustion chamber. Premixed combustion requires that the fuel and the oxidant have been mixed before combustion begins. In non-premixed combustion, the diffusion rate controls the process since the time required for convection and diffusion is greater than the time required for combustion reactions.

EXPERIMENTAL APPROACH

The experimental setup is shown in Figure 1(a), composed of a single-cylinder diesel engine tested at 1800 rpm, coupled to an electromagnetic dynamometer (Schenk, model W70). The main characteristics of the engine are given in Table 1. A piezoelectric pressure sensor (Kistler, model 6041A) was installed in the cylinder head, and its signal was synchronised with the incremental encoder to determine the in-cylinder pressure for each crank angle. The fuel consumption was measured using an electronic balance (Marte, model AD5000) with serial port communication. The instant reading of the data allowed the calculation of the fuel flow. The engine torque was measured with an extensometer type load cell installed on the dynamometer arm. The air admitted mass was measured with the hot-film air-mass meter (Bosch, model HFM 2).

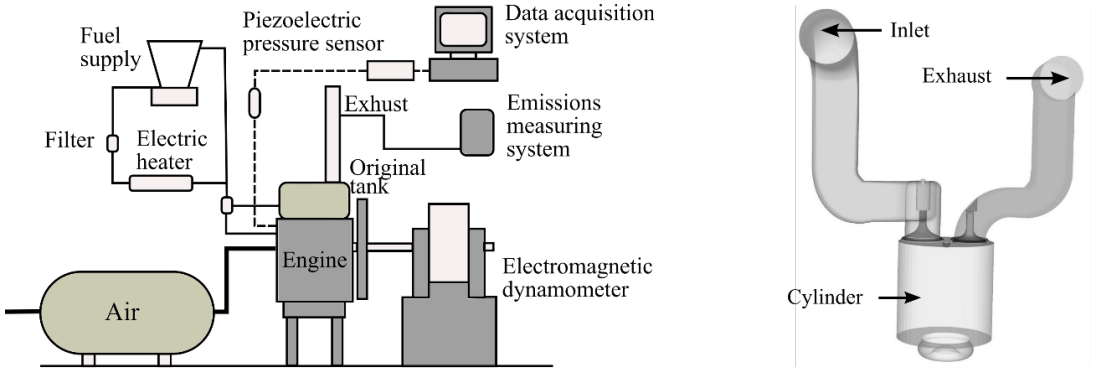

(a) (b)

Figure 1. (a) Setup of the experimental bench, and (b) three-dimensional geometry used in the simulation.

Table 1. Technical specifications of the diesel engine.

Item	Specification
Mark	Yanmar, model YT22E
Type	Diesel, 4 strokes, 1 cylinder
Injection system	Direct
Cylinder diameter	115 mm
Cylinder capacity	1194 cm^3
Compression ratio	17.3
Nominal power	14.7 kW/2200 RPM
Specific fuel consumption at nominal power	238 g/kW-h

The temperature-dependent thermophysical properties for the diesel fuel (commercial Brazilian diesel), were obtained from experimental measurements for density, dynamic viscosity and surface tension from a temperature range of 25 to 85°C and, existing data in the Converge CFD software, for thermal conductivity, vapour pressure, heat of vapourisation and specific heat. The in-cylinder pressure experimental data were utilised to validate results found through the numerical simulation of combustion. Also, this data was employed to calculate the in-cylinder temperature from a zero-dimensional thermodynamic model.

NUMERICAL APPROACH

The simulation of the intake and compression strokes and the spray combustion was carried out for a 4-stroke single-cylinder diesel engine, direct injection with compression ratio 17.3. The three-dimensional geometry of the engine is shown in Figure 1(b). For the intake and exhaust valve, the opening of each was obtained as a function of the crank angle. For the numerical solution of the equations governing the turbulent flow, structured real-time mesh generation was applied based on parameters given by the user. A fully implicit formulation was used in the time interpolation function. The pressure-velocity coupling used the PISO (Pressure Implicit with Splitting of Operators) algorithm [39], while the pressure solution used the multigrid method. To represent within the turbulent boundary layer the distributions of speed, temperature, energy etc., the Law of the Wall was used.

In the fuel spray simulation, the Blob model for a primary breakup and the Kelvin-Helmholtz and Rayleigh-Taylor (KH-RT) model for the secondary breakup (Eq.(11)) were applied, including the formation of new droplets without

breakup length [25], [27], [29], [40], [41]. For droplet collision, the No Time Counter (NTC) model and a dynamic droplet drag model were applied, including a dynamic discharge coefficient and the interaction of the droplets with the wall. To model the droplet size change due to evaporation, the Frossling correlation in Eq.(13) and the Rantz-Marshall model for heat transfer in droplet evaporation in Eq.(16) were used. In order to observe the influence of the breakup time τ_{KH}, on the variables of spray and fuel combustion, parameter B_1 was modified in the simulation using values of $B_1 = 7$, $B_1 = 50$ and $B_1 = 100$. In these three cases, the data for the standard simulation for diesel fuel corresponds to the simulation where $B_1 = 7$ is used.

The fuel injector has five nozzles of 0.3 mm diameter each. For the combustion simulation, the thermophysical properties of liquid fuel (mentioned in the experimental approach section), and the kinetic mechanism of n-dodecane ($C_{12}H_{26}$), with 106 species and 420 reactions (developed by Lawrence Livermore National Laboratory) were used. For NOx emissions, the extended mechanism of Zeldovich was used, and for soot formation, the Hiroyasu model coupled with the Nagle and Strickland-Constable-NSC model, was applied to simulate oxidation [42].

The mesh size independence on the numerical response of the flow field was verified to define the appropriate mesh size for the simulation of the intake and compression strokes. For this purpose, 6 mm, 4 mm and 3 mm base size meshes were used. Figure 2 shows the maximum in-cylinder pressure as a function of the crank angle for the engine simulation at 1800 rpm with three base mesh sizes tested. For the 6 mm mesh size, one observes a significant difference (9%) if compared to the values obtained using the 4 mm and 3 mm mesh sizes. The pressure line trend is maintained with the 4 mm mesh size, and its values are almost equal to that presented with the 3 mm mesh size.

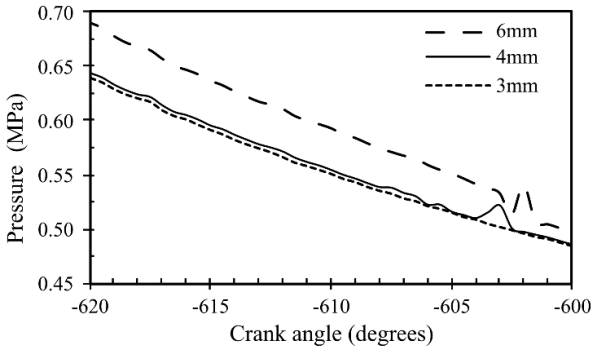

Figure 2. In-cylinder maximum pressure as a function of the crank angle for three mesh sizes.

A 4.0 mm base mesh was used for all axes. Using Adaptive Mesh Refinement (AMR) based on speed and temperature throughout the geometry, refining the mesh to 1.0 mm in regions of maximum speed and temperature gradient. A fixed embedding mesh refinement was performed on the inlet, exhaust and spray valves to a size of 0.5 mm. For each of the solid boundaries that form the system, the temperature was obtained from the heat transfer simulation in the engine, made in Converge CFD, with the conjugate head transfer model, for 25 engine cycles, [43]. The obtained values are listed in Table 2.

Table 2. Boundaries temperature.

Wall	Temperature (K)
Cylinder	455
Piston	445
Cylinder head	450
Intake	303
Exhaust	800

For the airflow inlet to the engine, experimental data of pressure measured as a function of crank angle and chemical species of the air were used. For the engine flow outlet, the conditions of temperature and chemical species (obtained experimentally according to [30]) were applied in addition to the atmospheric pressure. The engine geometry was divided into three regions: the cylinder, the intake duct and the exhaust duct. For the in-cylinder gases at the initial state, the pressure was measured experimentally in the engine, the temperature was obtained theoretically and the species were measured experimentally in the exhaust duct according to [30]. For the intake and exhaust ducts, the initial conditions applied for the pressure, temperature and species applied are shown in Table 3. The simulation was carried out at two stages, as follows:

i. The first stage simulates the intake and compression strokes, starting at -640° crank angle (before the exhaust) to advance the intake and compression stroke, ending at -20° crank angle, where the numerical solution of all variables (pressure, temperature, speed, chemical species and turbulent kinetic energy), was obtained.
ii. The second stage of fuel spray and combustion simulation started at -20°, using the values of the variables recorded at the end of the first stage and ending at 90°. The injection start angle (-15°) was determined using experimental pressure data, according to the methodology described by Tadros et al. [44], obtaining an injection period of 30°. The mass of injected fuel was experimentally determined, obtaining a value of 68.09 mg.

Table 3. Initial conditions.

Region	Pressure (kPa)	Temperature (K)	Species
Cylinder	921.9	1724	Experimental
Intake duct	Atm	360	Air species
Exhust duct	Atm	1100	Experimental

RESULTS AND DISCUSSION

The main phenomena and parameters present in the flow inside the motor were analysed, such as volumetric efficiency, discharge coefficient, flow structure, pressure field, temperature, and speed. The variables analysed for the fuel spray were average Sauter diameter, temperature, pressure, heat release rate and species formed in fuel evaporation and combustion. The values of the variables correspond to their averages in the different regions of the engine geometry.

Discharge Coefficient at the Intake and Volumetric Efficiency

Figure 3 shows the numerical result obtained for the behaviour of the instantaneous discharge coefficient C_{Di}, as a function of the crank angle. The total discharge coefficient (C_D) was 0.51. By comparing air mass flow into the cylinder, calculated isentropically and numerically, it was found that in the middle of the admission stroke, the maximum isentropic mass flow was 0.28 kg/s, and the maximum numerical mass flow was 0.12 kg/s.

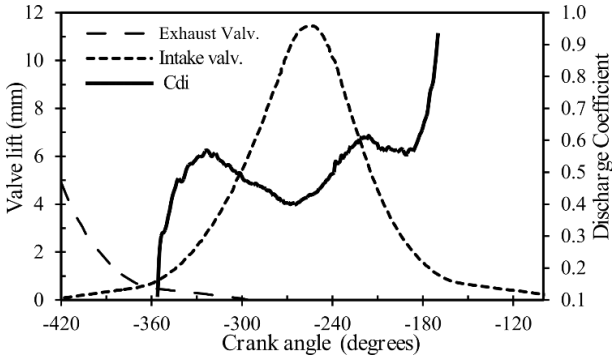

Figure 3. Instantaneous discharge coefficient as a function of the crank angle.

At the beginning of the intake, there is an output of combustion products to the intake line due to valves overlapping [10]. Furthermore, in the results of the simulation inside the cylinder, a maximum gas mass of 1.128E-3 kg was obtained, when the piston was at the end of the admission stroke. Then, since the intake valve was not yet closed, a mass return from the cylinder to the intake manifold of 3.737E-5 kg was obtained, leaving finally 1.091E-3 kg in the cylinder. This represents 3.4% of mass returns to the intake manifold before the intake valve closes. In theory, the mass of air enters engine cylinder is equal to the product between the density of the air and the volume displaced by the piston, at the conditions of temperature and atmospheric pressure of the place. Under real operating conditions, this does not happen because of the short time in each cycle, the restrictions in the intake pipe and the presence of the valves. Therefore, less air mass enters the cylinder than the ideal amount. The volumetric efficiency of the engine obtained was $\eta_v = 78.1\%$. This value is similar to that obtained by Subramanian et al. [14].

Figure 4 shows the speed vectors obtained in the simulation, for a valve lift of 3.0 mm, at the beginning of the intake. Here, it is observed that the gas in its passage through the valve has speeds near 140 m/s, so a conical ring jet is formed, and the flow reaches high Reynolds numbers, allowing the jet to reach the piston head and cylinder walls; forming vortices due to the interaction with these surfaces [16]. Furthermore, inside the cylinder, the mass movement is rotational, generated mainly by the intake geometry, the valve and the piston geometry. On the intake stroke, vortices are formed in the centre of the cylinder because the intake valve is not centred in the cylinder, and smaller vortices are also generated as a result of the larger vortex.

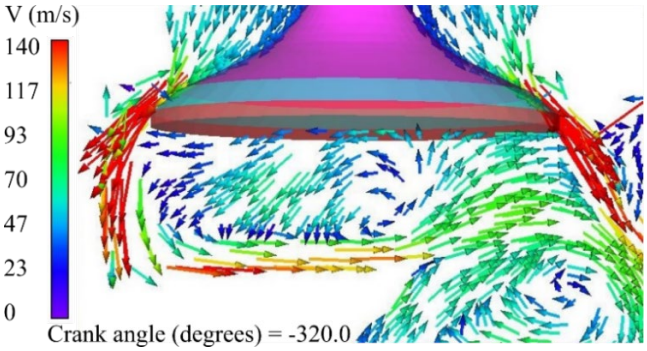

Figure 4. Air speed at the intake and inside the cylinder.

When the intake valve closes, pressure waves in the intake duct remain with oscillating effects of negative pressures (below atmospheric pressure) or positive pressures (above atmospheric pressure) for the next intake process. The amplitudes of the pressure oscillations depend on the length of the intake duct, with the amplitude at the points farthest from the valve (Intake duct inlet) being smaller and the amplitude at the point closest to the valve (Intake valve) greater, as shown in Figure 5.

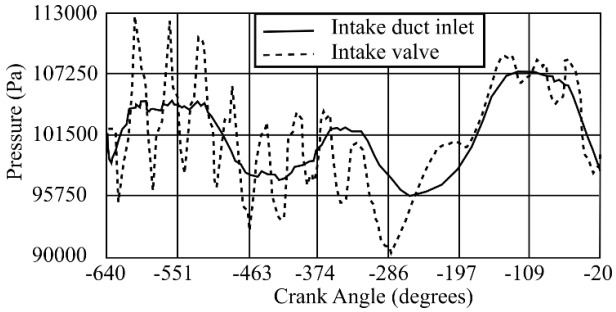

Figure 5. Pressure fluctuations in the engine intake duct as a function of crank angle.

Swirl and Tumble Ratio

The numerical results showed that at the beginning of the intake (-360°), the swirl ratio (R_s) has negative values, and then its value increases in the second half of the intake, decreasing slightly during the beginning of the compression due to the effects of viscous drag with the cylinder walls and the piston. Its maximum value was obtained at the end of compression, as can be seen in Figure 6. These results are similar to those obtained by [14], [19], where these maximum values occur in compression due to the shape of piston head. According to Figure 6, the tumble ratio in x (R_{tx}) increases rapidly at the beginning of the intake and then decreases. In the middle of the intake stroke, the flow generated by the valve at the intake forms opposite rotating vortices at different points in the cylinder, as shown in Figure 4. The tumble ratio in y (R_{ty}) shown in Figure 6 increases rapidly at the beginning of the intake and then decreases, remaining constant until the first half of the compression stroke.

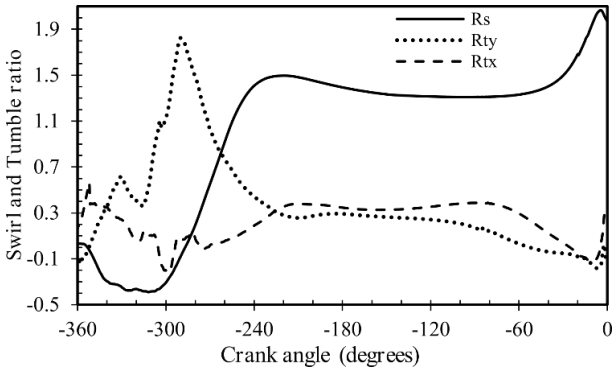

Figure 6. Swirl and tumble ratio as a function of crank angle.

Figure 7(a) shows the velocity vectors for a negative swirl ratio (-0.4), at the beginning of the intake at a crank angle of -320°, while Figure 7(b) shows the end of the compression stroke for a crank angle of -20°, where the swirl ratio is positive (1.9). This behaviour is consistent with that shown by Heywood [8]. Therefore, in the direct injection engine, the swirl is used to obtain a fast fuel-air mixture because, when the piston in the compression is close to TDC, the swirl increases, improving the air intake to the combustion chamber. In the compression stroke, near the TDC (-20°), for the yz plane in the combustion chamber, two opposite vortices are formed, which coincides with the modelling done by Payri et al. [19] and with that described by Heywood [8].

Turbulent Kinetic Energy and Dissipation of Turbulent Kinetic Energy

The turbulent kinetic energy within the cylinder is low at the beginning of the intake and reaches a maximum value at a crank angle of approximately -270°, as can be seen in Figure 8(a). After this point, it decreases, returning to values close to zero at the end of the compression. The formation and destruction of k is related to the rate of dissipation of turbulent kinetic energy (ϵ). In Figure 8(a) and 8(b), it can be seen that k values are high when ϵ is also high. The value of ϵ depends on the turbulent length scale, which, as it increases, makes ϵ decrease rapidly. The turbulent length scale has a large increase in intake at the stage of greatest cylinder filling and where the swirl has the greatest increase. The greatest fluctuations in cylinder speed occur where the highest k is obtained, in this case, at the mid-point of the admission stroke, which coincides with the results obtained by [19].

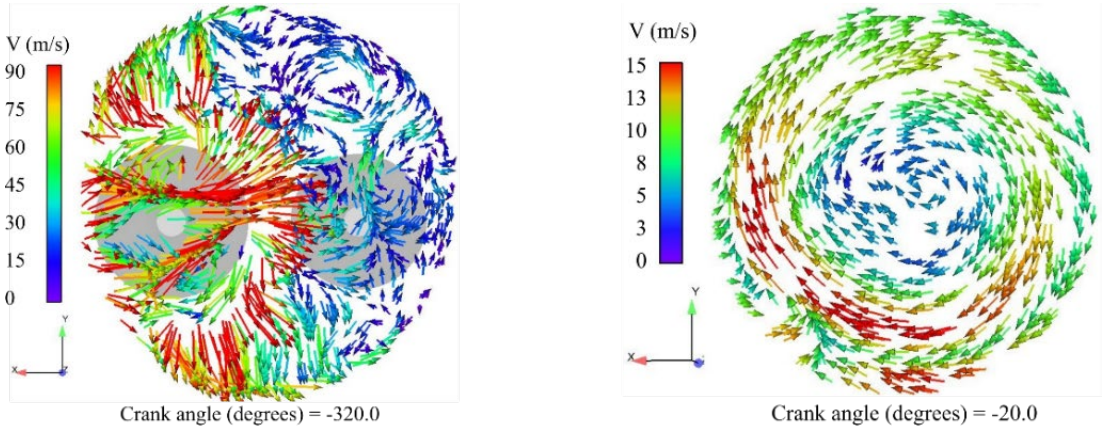

(a) (b)

Figure 7. Speed vectors in the cylinder around z-axis at the (a) beginning of intake and (b) end of compression.

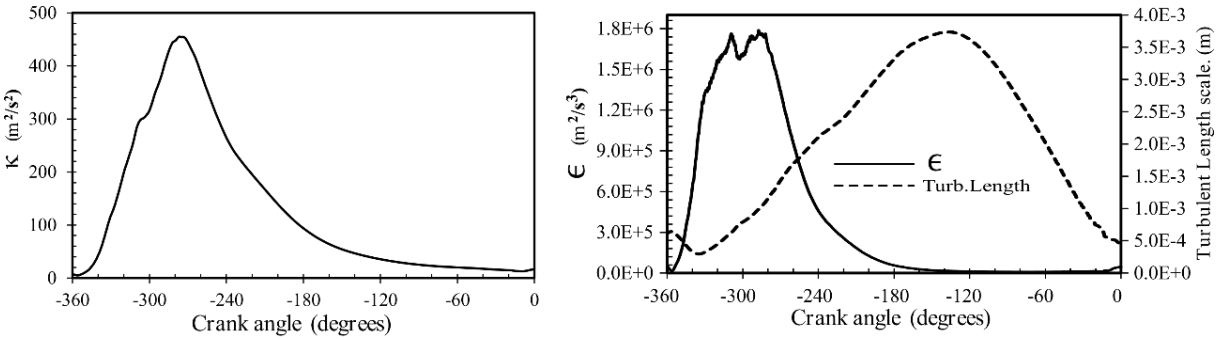

(a) (b)

Figure 8. (a) Turbulent kinetic energy (TKE) as a function of crank angle, and (b) dissipation of turbulent kinetic energy (ESP) as a function of crank angle.

In-Cylinder Pressure and Temperature

The numerical model was validated by comparing the experimental and numerical in-cylinder pressure, considering diesel fuel. The comparison of the in-cylinder temperature calculated with a zero-dimensional model and numerically is also made. In the combustion simulation, for three break times τ_{KH} in the KH-RT model, the factor B_1 is modified using values of $B_1 = 7$, $B_1 = 50$ and $B_1 = 100$. The pressure behaviour inside the cylinder for each of the values of B_1 can be seen in Figure 9. Furthermore, it can be seen that pressure reaches a maximum value at TDC, and the experimental pressure in the engine has a higher value than the numerical pressure for the three values of B_1. The experimental pressure and the numerical pressure with $B_1 = 7$ have the closest values, and between them, the maximum difference is presented at a crank angle of 6.5°, with a value of 10%. After -4.4°, the trend of all pressure lines, including the experimental one, changes and it is evident that the pressure decreases when the value of B_1 increases. The above is a consequence of the breakup time since large values decrease the combustion. The concordance between the experimental and numerical data indicates that the numerical method and the models used in this work are adequate to perform subsequent representative combustion analyses with values of $B_1 = 7$.

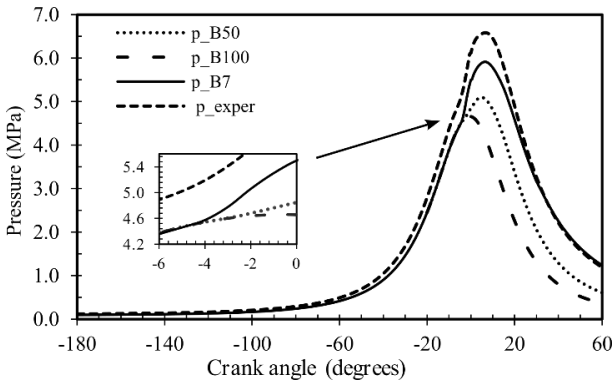

Figure 9. Pressure in the cylinder for three values of $\boldsymbol{B_1}$, as a function of crank angle.

Figure 10 shows the in-cylinder temperature variation, calculated with the 0-dimensional isentropic model ($T_{isentrop}$), and the numerical temperature, for the three values of B_1. There, isentropic temperature and the numerical temperature

for $B_1 = 7$ show approximately equal values after the start of combustion. The temperature varies from -9.0° for the different values of B_1, where it is observed that it increases in the case of the two smaller values of B_1, and for $B_1 = 100$, the slope does not change. This change in the slope of the temperature lines occurs at approximately the same crank angle at which the pressure line slope change occurs.

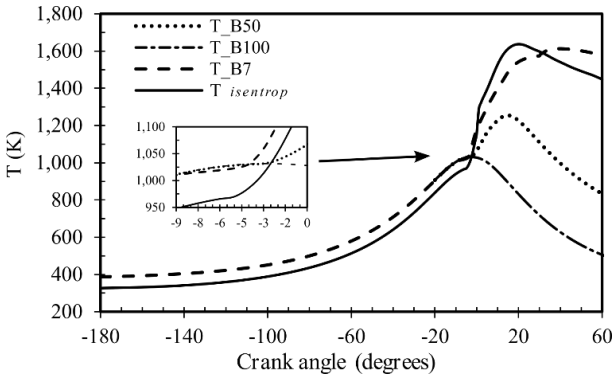

Figure 10. Temperature in the cylinder for three values of B_1, as a function of crank angle.

With respect to this analysis, discrepancies may be the result of uncertainties in injection parameters, such as injection pressure, velocity and time. In general, the model was able to replicate the general trends of in-cylinder pressure and temperature as a function of the crank angle, showing agreement between the experimental and numerical data. Consequently, this model will be used as a baseline for subsequent simulations in which spray combustion will be considered and added to analyse the influence of the physical properties of liquid fuel in the engine for alternative fuels.

Droplet Breakup and Evaporation

Figure 11 shows the average Sauter diameter for each of the values of B_1. There, it is observed that in the primary breakup, initial drops of 0.3 mm diameter are formed, and then the secondary breakup process starts where the KH-RT breakup mechanism acts. Furthermore, it is observed that the secondary breakup for each one of the cases starts in different crank angles, as in Table 3. Therefore, there are different regions in the breakup process. From the beginning of the secondary breakup, the diameter of the droplets decreases faster for values of $B_1 = 7$, reaching a diameter value of 0.29 mm at crank angles shown in Table 3. After the droplet reaches 0.29 mm diameter, the trend of all three cases is similar, but in the case of $B_1 = 7$ the droplet reaches smaller diameters in less time. As the breakup time increases, the droplet diameter is larger throughout the simulation; therefore, the number of particles in the computational domain decreases, causing greater spray penetration by the particle impulse.

Figure 12 describes the behaviour of the heat release rate (HR) in J/time, where it is observed that for high values of B_1 this rate decreases. For the simulation, it was considered that ignition occurs when the RH reaches a positive value, which is obtained from the crank angles shown in Table 3.

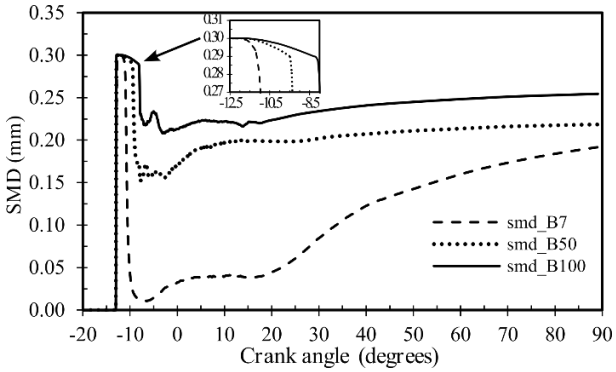

Figure 11. Average Sauter diameter of the droplet for three values of B_1, as a function of the crank angle.

Table 3. Droplet breakup analysis and ignition.

B_1	Pressure (kPa)	Temperature (K)	Species
7	-11.78°	-11.00°	-9.58°
50	-11.38°	-9.48°	-8.58°
100	-11.38°	-8.48°	-6.48°

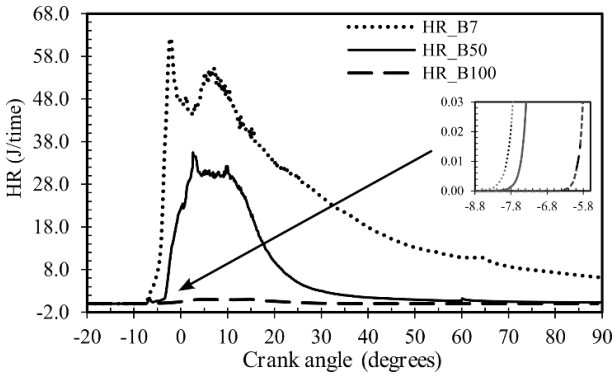

Figure 12. Heat release rate for three values of $\boldsymbol{B_1}$, as a function of crank angle.

In the numerical simulation, fuel evaporation is identified when the mass of the chemical species dodecane ($C_{12}H_{26}$) is present. Figure 13 describes the presence of mass fraction of ($C_{12}H_{26}$) as a function of the crank angle, where it is evident that for $B_1 = 7$ the evaporation increases rapidly at an angle of -10.6°, this being the highest mass presence. When comparing this result with the case of $B_1 = 100$ (which is the lowest mass, evaporation is presented in -7.9°, which represents a delay of 2.7° in relation to the simulation with $B_1 = 7$. Accordingly, the evaporation rate is influenced by constant B_1. Furthermore, it is evident that after the first peak for the three values studied, the mass fraction decreases due to premixed combustion.

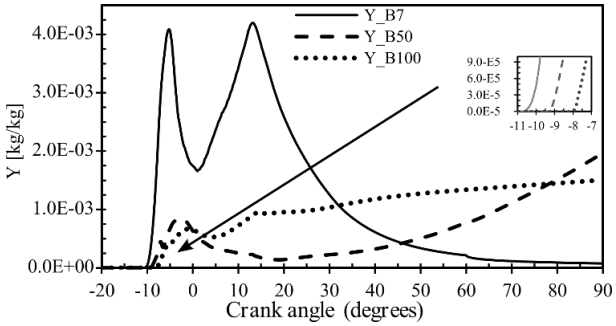

Figure 13. Mass fraction of $\boldsymbol{C_{12}H_{26}}$ for three values of $\boldsymbol{B_1}$, as a function of crank angle.

To identify the beginning of combustion (with a parameter other than HR), the analysis of mass fraction behaviour of chemical species, which are formed in the first reactions of the kinetic mechanism when combustion occurs or on the ignition, was carried out. The results obtained are shown in Figure 14(a), where it is evident that the formation of the species OH is greater for low values of B_1. Figure 14(b) shows that the formation of HO_2 is not much influenced by parameter B_1, even if its formation is present at different points; -8.4° for $B_1 = 7$, -8.0° for $B_1 = 50$ and -7.0° for $B_1 = 100$. Once this species is formed, for the values $B_1 = 50$ and $B_1 = 100$ as opposed to the value $B_1 = 7$, it remains and does not react in premixed combustion. Figure 14(c) shows parameter B_1 has a great influence on the species H_2O_2, since for low values of B_1, this species is generated, and then the mass fraction decreases, but for $B_1 = 100$, the mass fraction of this species always increases, there being no decrease in it. This makes it possible to define that the formation of H_2O_2, begins at the same point where the production of fuel vapour is generated for a value of $B_1 = 7$, (-10.6°) (see Figure 13). Finally, Figure 14(d) shows the result obtained for the species CO, where it is evident that it is quite influenced in its formation by parameter B_1 since when the value of this parameter increases, the formation of this species decreases. Its formation is rapid for $B_1 = 7$, starting at -7.4°, at -7.0° for $B_1 = 50$ and at -5.6° for $B_1 = 100$. This makes it possible to define that the formation of CO starts at the same point where the production of fuel vapour is generated for a value of $B_1 = 7$ (-10.6°) (see Figure 13).

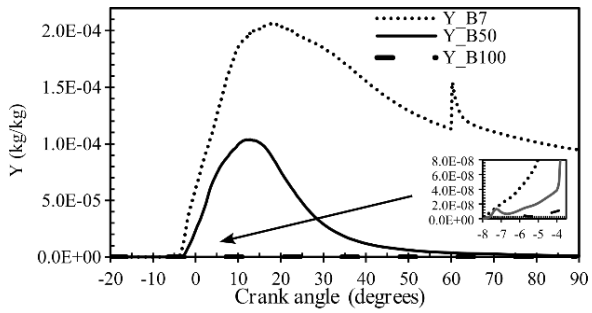

(a)

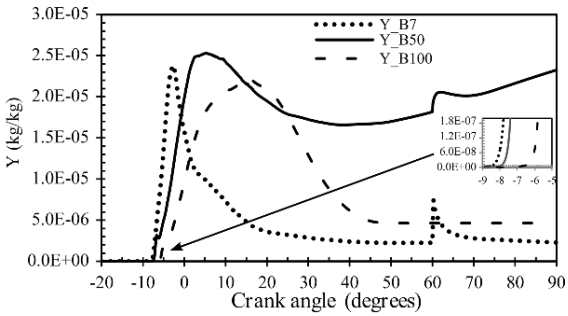

(b)

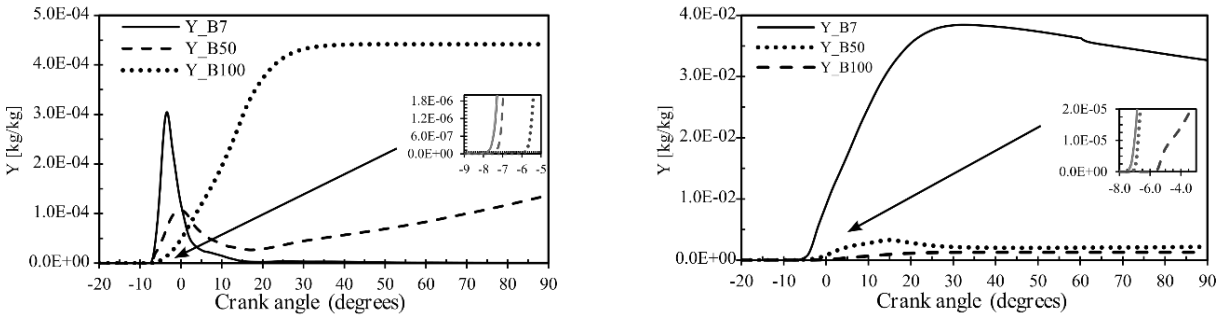

Figure 14. Mass fraction of chemical species for three values of $\boldsymbol{B_1}$ as a function of the crank angle (a) Mass fraction of OH, (b) Mass fraction of $\mathbf{HO_2}$, (c) Mass fraction of $\mathbf{H_2O_2}$, (d) Mass fraction of CO.

CONCLUSION

The data obtained in the simulation for the admission and compression strokes show that the fields in the flow within the cylinder fit the existing experimental data of pressure and the numerical data obtained by other authors, which provides a proper validation of the model developed in this work by its authors. The configuration of the piston of the simulated engine contributes to increasing the swirl at the end of the compression, which favours the formation of the fuel-air mixture. This increase in swirl is generated when the piston is close to the TDC on compression, as a result of the shape of the piston head. The validation of the model for these strokes in the engine ensures that the new phase of fuel spray and combustion simulation in the engine is also correct, as the results obtained in this work are important for the development of the spray and combustion that will be addressed in subsequent work.

In the engine, when the piston approaches TDC during compression, the volume around the other axes of the combustion chamber is reduced to a minimum, and then the gas is forced to enter the combustion chamber radially, generating a tumble near the external axis of the piston crown, which is desirable to spread the combustion flame as quickly as possible. When the droplet breakup time is altered by means of parameter B_1 of the KH breakup model, the fuel droplets, which are the result of the secondary break, will be of larger diameter for values greater than B_1. After studying three values of the breakup time constant (B_1), the results indicate that for a value of B_1 = 7, the numerical method and the models used are adequate to analyse diesel spray combustion. It was shown that parameter B_1 influences the formation of the spray, evaporation, ignition and combustion, since having higher values of B_1 delays evaporation and similarly the formation of species, delaying ignition and the formation of the fuel-air mixture.

ACKNOWLEDGEMENT

The authors are grateful to Laboratório de Combustão e Engenharia de Sistemas Térmicos (LabCET) of The Universidade Federal de Santa Catarina, Brazil, for allowing for conducting experimental work need for the current research. Also grateful to Mechanical Technology Research Group of Technological University of Pereira, and the Mechanical Engineering Research Group of Pamplona University (GIMUP) from Colombia, for their support in conducting experiments and simulations.

REFERENCES

[1] M. H. Ali *et al.*, "Cyclic pressure variations in a small diesel engine fueled with biodiesel and antioxidant blends," *Int. J. Automot. Mech. Eng.*, vol. 17, no. 2, pp. 7851–7857, 2020, doi: 10.15282/ijame.17.2.2020.04.0585.

[2] C. B. How, N. M. Taib, and M. R. A. Mansor, "Performance and exhaust gas emission of biodiesel fuel with palm oil based additive in direct injection compression ignition engine," *Int. J. Automot. Mech. Eng.,* vol. 16, no. 1, pp. 6173–6187, 2019, doi: 10.15282/ijame.16.1.2019.7.0469.

[3] S. Dey, M. Deb, and P. K. Das, "An investigation of diesohol-biodiesel mixture in performance-emission characteristics of a single cylinder diesel engine: A trade-off benchmark," *Int. J. Automot. Mech. Eng.*, vol. 16, pp. 7467–7479, 2019, doi: 10.15282/ijame.16.4.2019.18.0552.

[4] W. Anggono *et al.*, "Effect of Cerbera manghas biodiesel on diesel engine performance," *Int. J. Automot. Mech. Eng.*, vol 15, no. 3, pp. 5667–5682, 2018, doi: 10.15282/ijame.15.3.2018.20.0435.

[5] S. Pai, A. Sharief, and S. Kumar, "Influence of ultra injection pressure with dynamic injection timing on CRDI engine performance using simarouba biodiesel blends," *Int. J. Automot. Mech. Eng.,* vol. 15, no. 4, pp. 5748–5759, 2018, doi: 10.15282/ijame.15.4.2018.3.0440.

[6] A.K. Mohamed Farmaan *et al.*, "Experimental and computational investigation of engine characteristics in a compression ignition engine using mahua oil", *Fuel*, vol. 284, 2021, 119007, doi:10.1016/j.fuel.2020.119007

[7] S. Shaik. Khasim, B. Nageswara Rao, and J. Donepudi, "Computational fluid dynamic analysis of Nodularia Spumigena Microalgae biodiesel and Karanja biodiesel blends using ANSYS in CI engine", *Mater. Today: Proc.*, vol. 27, no.2, 2020, pp. 1812-1820, doi:10.1016/j.matpr.2020.03.781

[8] J. B. Heywood, *Internal combustion engines fundamentals*. United States of America: McGraw-Hill, 1988.

[9] W. W. Pulkrabek, *Engineering fundamentals of the internal combustion engine*. United States of America: Prentice Hall, 1997.

[10] *Converge v2.3 Manual.* Convergent Science, Inc., 2016.

[11] J. Hemanandh, *et al*. "Robust design approach for intake manifold of the 1 litre turbo charger intercooler diesel engines", *Int. J. Ambient Energy*, vol. 41, no.11, pp. 1214-1226, 2020, doi: 10.1080/01430750.2018.1507935

[12] D. Malkhede and H. Khalane. "Maximizing volumetric efficiency of IC engine through intake manifold tuning". In SAE 2015 World Congress & Exhibition, 2015, doi: 10.4271/2015-01-1738.

[13] H. K. Nguyen *et l.,* "Simulation environment for analysis and controller design of diesel engines", *IFAC-PapersOnLine*, vol. 53, no. 2, pp. 13970-13975, 2020, doi: 10.1016/j.ifacol.2020.12.915.

[14] S. Subramanian *et al.,* "Piston bowl optimization for single cylinder diesel engine using CFD", SAE Technical Paper, 2016, doi: 10.4271/2016-28-0107.

[15] F. Perini *et al.*, "Piston geometry effects in a light-duty, swirl-supported diesel engine: Flow structure characterization", *Int. J. Engine Res.*, 2018; vol. 19, no.10, pp. 1079-1098. doi:10.1177/1468087417742572.

[16] G. Rathore, A. Goel, and S. Choudhary, "Numerical study of in-cylinder flow using screw threaded intake manifold in a single cylinder diesel engine", *SAE Technical Paper*, 2016, doi: 10.4271/2016-28-0136.

[17] R. K. Maurya and P. Mishra, "Parametric investigation on combustion and emissions characteristics of a dual fuel (natural gas port injection and diesel pilot injection) engine using 0-D SRM and 3D CFD approach", *Fuel*, vol. 210, pp. 900-913, 2017, doi: 10.1016/j.fuel.2017.09.021

[18] M. Gold *et al.*, "Simulation and measurement of transient fluid phenomena within diesel injection", SAE Technical Papers 2019-01-0066, 2019, doi: 10.4271/2019-01-0066.

[19] F. Payri *et al.,* "CFD modeling of the in-cylinder flow in direct-injection Diesel engines," *Comput. Fluids*, vol. 33, no. 8, pp. 995–1021, 2004, doi: 10.1016/j.compfluid.2003.09.003.

[20] S.-C. Kong, Z. Han, and R. D. Reitz, "The development and dpplication of a diesel ignition and combustion model for multidimensional engine simulation," SAE Technical Papers 1995-02-01, 1995, doi: 10.4271/950278.

[21] T. Yao *et al.,* "A compact skeletal mechanism for n-dodecane with optimized semi-global low-temperature chemistry for diesel engine simulations", *Fuel,* vol. 191, pp.339-349, 2017, doi: 10.1016/j.fuel.2016.11.083.

[22] A. L. Delgado-Mejia y L. C. Olmos-Villalba, "Heptane and Dodecane as surrogates of diesel fuel, a comparison with Computational Fluid Dynamics (CFD)", *Revista Cintex*, vol. 20, no. 1, pp. 97-110, 2015.

[23] A. Wehrfritz *et al.,* "Large Eddy simulation of n-dodecane spray flames using Flamelet Generated Manifolds", *Combustion and Flame*, vol. 167, pp 113-131, 2016, doi: 10.1016/j.combustflame.2016.02.019.

[24] T. Tulwin, M. Wendeker and Z. Czyż, Zbigniew. "The swirl ratio influence on combustion process and heat transfer in the opposed piston compression-ignition engine", *Combustion Engines*, 170(3), pp 3-7, 2017, doi: 10.19206/CE-2017-301.

[25] L. Zhou *et al.*, "Large eddy simulation of spray and combustion characteristics with realistic chemistry and high-order numerical scheme under diesel engine-like conditions," *Energy Convers. Manag*., vol. 93, pp. 377–387, 2015, doi: 10.1016/j.enconman.2015.01.033.

[26] M. Yousefifard, P. Ghadimi, S. M. Mirsalim, "Probing into the effects of fuel injection pressure and nozzle hole diameter on spray characteristics under ultra-high injection pressures using advanced breakup model", *Scientia Iranica*, 23(1), pp 238-248, 2016.

[27] Y. Gao et al., "Breakup, instabilities, and dynamics ofhigh-speed droplet under transcritical conditions," *Adv. Mech. Eng.*, vol. 7, no. 6, pp. 1–15, 2015, doi: 10.1177/1687814015588469.

[28] S. Srivastava and F. Jaberi, "Large eddy simulations of complex multicomponent diesel fuels in high temperature and pressure turbulent flows," *Int. J. Heat Mass Transf.*, no. 104, pp. 819–834, 2017, doi: 10.1016/j.ijheatmasstransfer.2016.07.011.

[29] D. Kim, J. Martz, and A. Violi, "Effects of fuel physical properties on direct injection spray and ignition behavior," *Fuel*, no. 180, pp. 481–496, 2016, doi: 10.1016/j.fuel.2016.03.085.

[30] N. A. N. Garzón, "Experimental and exergetic analysis of the operation of a diesel engine with vegetable oil (in Portuguese)," Federal University of Santa Catarina, Brazil, 2012.

[31] E. Marlina, I. Wardana, L. Yuliati and W. Wijayanti, "The effect of fatty acid polarity on the combustion characteristics of vegetable oils droplets", *Mater. Sci. Eng.,* vol. 494, 2019, doi:10.1088/1757-899X/494/1/012036

[32] A. S. Zongo et al., "The effect of atmospheric oxygen on the puffing and bursting phenomena during vegetable oils droplets vaporization process for their use as biofuel in diesel engine", *Energy Power Eng.*, vol. 10, no. 12, pp. 518-533, 2018. doi: 10.4236/epe.2018.1012033

[33] *Converge v2.3 Manual,* Convergent Science, Inc., 2016.

[34] A. Bejan, *Convection heat transfe*r, 4th ed. United States of America: John Wiley & Sons, Inc., 2013.

[35] D. Wilcox, *Turbulence modeling for CFD,* 2nd ed. New York, Unites States, 1993.

[36] K. Kuo and R. Acharya, *Fundamentals of Turbulent and multiphase combustion*. United States of America: John Wiley & Sons, Inc, 2012.

[37] A. H. Lefebvre, *Atomization and sprays*, 1st ed. United States of America: Taylor and Francis Group, 1989.

[38] R. Reitz, "Modeling atomisation processes in high-pressure vaporising sprays," *At. Sprays*, vol. 3, pp. 309-337, 1988.

[39] H. K. Versteeg and W. Malalasekera, *An introduction to computional fluid dynamics*. United States of America: John Wiley and Sons Inc, 1995.

[40] C. Baumgarten, *Mixture formation in internal combustion engines*. Germany: Springer, 2006.

[41] Y. Shi, H.-W. Ge, and R. D. Reitz, *Computational optimisation of internal combustion engines*. United States of America: Springer, 2011.

[42] S. R. Turns, *An introduction to combustion*, 2nd ed. United States of America: McGraw-Hill, 2000.

[43] Y. Ortiz, E. G. Florez, and J. C. Serrano, "Multidimensional simulation of heat transfer in an internal combustion compression-ignition engine," *Int. J. Mech. Eng. Technol.*, vol. 10, no. 11, pp. 307–317, 2019.

[44] M. Tadros, M. Ventura, and C. Guedes Soares. "Assessment of the performance and the exhaust emissions of a marine diesel engine for different start angles of combustion". *Marit. Technol. Eng.*, vol. 3, pp.769-775, 2016.